Science Bulletin 64 (2019) 261–269

Contents lists available at ScienceDirect

Science Bulletin

journal homepage: www.elsevier.com/locate/scib

Article

Necklace-like Si@C nanofibers as robust anode materials for high performance lithium ion batteries

Xiangzhong Kong [a], Yuchao Zheng [a], Yaping Wang [a], Shuquan Liang [a], Guozhong Cao [c], Anqiang Pan [a,b,*]

[a] School of Materials Science & Engineering, Central South University, Changsha 410083, China
[b] Key Laboratory of Nonferrous Metal Materials and Engineering Ministry of Education, Central South University, Changsha 410083, China
[c] Department of Materials Science & Engineering, University of Washington, Seattle, WA 98195, USA

ARTICLE INFO

Article history:
Received 29 October 2018
Received in revised form 28 December 2018
Accepted 2 January 2019
Available online 30 January 2019

Keywords:
Necklace-like
Carbon shells network
N-doped
Mesoporous silicon
Lithium ion batteries

ABSTRACT

Silicon is believed to be a promising anode material for lithium ion batteries because of its highest theoretical capacity and low discharge potential. However, severe pulverization and capacity fading caused by huge volume change during cycling limits its practical application. In this work, necklace-like N-doped carbon wrapped mesoporous Si nanofibers (NL-Si@C) network has been synthesized via electrospinning method followed by magnesiothermic reduction reaction process to suppress these issues. The mesoporous Si nanospheres are wrapped with N-doped carbon shells network to form yolk-shell structure. Interestingly, the distance of adjacent Si@C nanospheres can be controllably adjusted by different addition amounts of SiO_2 nanospheres. When used as an anode material for lithium ion batteries, the NL-Si@C-0.5 exhibits best cycling stability and rate capability. The excellent electrochemical performances can be ascribed to the necklace-like network structure and N-doped carbon layers, which can ensure fast ions and electrons transportation, facilitate the electrolyte penetration and provide finite voids to allow large volume expansion of inner Si nanoparticles. Moreover, the protective carbon layers are also beneficial to the formation of stable solid electrolyte interface film.

1. Introduction

Lithium ion batteries (LIBs) with high energy density have drawn much attentions due to the ever-growing demand for technological applications, such as electric vehicles, portable electronics and renewable power stations [1–5]. The energy density of LIBs can be improved by using electrode materials with high theoretical capacities and proper working potentials [6–8]. Among various anode materials, silicon (Si) can be considered to be one of the most promising candidates because of its high theoretical capacity (4,200 mAh g^{-1} if $Li_{4.4}Si$), low discharge potential (0.5 V vs. Li/Li^+), natural abundance and environmental benign [9–11]. However, the poor intrinsic electronic conductivity and severe volume expansion (about 400%) hinder the practical application of Si based materials [12,13]. Such dramatic volume changes during lithiation-de-lithiation process often result in serious structural degradation, and regeneration of unstable solid electrolyte interface (SEI) on fractured Si surfaces via irreversible side reactions, thereby, leading to fast capacity fading [14–16].

To date, great efforts have been endeavored to address the above-mentioned problems. Various Si nanostructures, such as nanowires [17], nanosheets [18], nanorods [19], and hollow and porous structures [20] have been reported with improved electrochemical properties. Compared with bulks, nanostructures can shorten the ionic diffusion pathway and better accommodate the volume changes upon repeated cycles, thus better rate capability and cyclic stability can be obtained [11,21,22]. However, the large volume changes always cause the destruction and regeneration of the SEI layer, which result in the continuous consumption of electrolyte and the resistance increase at the interface between electrolyte and electrode [23–25]. Surface coating has been considered an effective approach to solve this problem, such as carbon coating to make the core-shell structured composites [26–30]. The carbon shell is beneficial to improving conductivity and accommodating the volume changes of Si to a limited degree [31,32]. Furthermore, a stable SEI layer can be formed on the carbon shell rather than the surface of Si, preventing the continual rupturing of the SEI film [33–37]. The interior void space of yolk-shell Si/C composites can relieve the elevated mechanical stress on the carbon shells during the expansion of inner Si nanoparticles, resulting in prolonged cycling stability

* Corresponding author.
E-mail address: pananqiang@csu.edu.cn (A. Pan).

https://doi.org/10.1016/j.scib.2019.01.015
2095-9273/

[38]. For instance, Yu and co-workers [34] reported dual functionalized double carbon shells coated Si nanoparticles, which delivers a capacity of 584 mAh g^{-1} after 200 cycles at 5 C. The inner carbon shell provides extra voids for Si expansion whereas the outer carbon shell stabilizes the SEI layer. Guo and co-workers [39] designed Si@void@C composite to boost lithium storage. Dou and co-workers [36] reported yolk-shell silicon-mesoporous carbon anode with a capacity of 500 mAh g^{-1} after 400 cycles at 420 mA g^{-1}. Compared with isolated Si/C nanoparticles, interconnected network structure can provide continuous three-dimensional (3D) conductive framework for fast electrons transport in all directions, resulting in better electric conductivity [40–44]. Furthermore, embedding Si nanoparticles into network structure can greatly improve mechanical strength and avoid agglomerations during cycling [33]. Therefore, it is essential to develop mesoporous network with yolk-shell structure to enhance the electrochemical performances of Si-based materials.

Herein, we design a necklace-like N-doped carbon wrapped mesoporous Si nanofibers (NL-Si@C) network for LIBs. The mesoporous Si nanospheres are encapsulated into N-doped carbon shells network to form a yolk-shell structure. Moreover, the carbon wrapped Si nanospheres are connected each other to form necklace-like nanofibers. The as-prepared structure has many superiorities: (1) the mesoporous Si nanospheres within the carbon shell can facilitate the electrolyte penetration and offer interior space for Si expansion; (2) the carbon shells avoid the direct contact between Si and electrolyte and thus are helpful to the formation of a stable SEI film; (3) necklace-like nanofiber network structure avoids the aggregations of Si@C nanospheres and provides continuous conductive pathway for fast electrons transportation in all directions. When utilized as anodes for LIBs, the necklace-like Si@C composites exhibit excellent electrochemical performances.

2. Experimental

2.1. Synthesis of SiO_2 nanospheres

SiO_2 nanospheres were synthesized by a Stöber process [45]. In a typically synthesis, 4.2 mL tetraethyl orthosilicate (TEOS) was added into a mixture solvent of 80 mL ethanol and 24 mL ammonium aqueous solution (30%), followed by vigorous stirring at room temperature for 1 h. The obtained SiO_2 nanospheres were centrifugally separated from the suspension and washed with deionized water and ethanol several times before drying in air at 70 °C overnight.

2.2. Synthesis of SiO_2@polymer network

SiO_2 nanospheres were dispersed in 2 mL *N*,*N*-dimethylformamide (DMF) homogeneously by ultrasonication for 30 min. Then, 0.2 g polyacrylonitrile (PAN, M_w = 150,000, Sigma-Aldrich Co.) was added into the dispersion with continuous stirring for 12 h. The obtained white suspension was transferred into a 5 mL injection syringe followed by electrospinning treatment. The voltage between the needle and the aluminum foil collector was set as 9.0 kV and the distance was 15 cm. The injection speed was controlled at 1 mL h^{-1}. Different amounts of SiO_2 nanospheres (0.1, 0.3, 0.5, and 0.7 g) were used for the electrospun and the obtained samples were designated as SiO_2@polymer-0.1, SiO_2@polymer-0.3, SiO_2@polymer-0.5 and SiO_2@polymer-0.7, respectively. The as-spun samples were heated in air at 250 °C for 60 min.

2.3. Synthesis of NL-Si@C network

The stabilized samples were mixed with Mg powder and NaCl in a mass ratio of 1:0.9:10. Then, the mixture was annealed in an inert atmosphere of Ar at 650 °C for 6 h with a ramping rate of 3 °C min^{-1}. The resulting products were washed with de-ionized water and 1 mol L^{-1} HCl to remove NaCl, Mg_2Si and MgO, respectively. After drying at 70 °C overnight, the obtained products are denoted as NL-Si@C-0.1, NL-Si@C-0.3, NL-Si@C-0.5 and NL-Si@C-0.7, respectively.

2.4. Synthesis of Si-C and Si-S

For comparison, monodisperse carbon coated Si nanospheres (Si-C) and Si nanospheres (Si-S) were also prepared by similar magnesium reduction of SiO_2@resorcinol-formaldehyde (RF) and SiO_2 nanospheres, respectively. To prepare SiO_2@RF, 1 g SiO_2 nanospheres were dispersed in a solution containing 70 mL deionized water and 30 mL ethanol under ultrasonication for 30 min. After that, 2.3 g hexadecyl trimethylammonium bromide (CTAB), 0.35 g resorcinol, 0.1 mL ammonium aqueous solution and then 0.5 mL formaldehyde solution were added into the SiO_2 dispersion under stirring. Then, the SiO_2@RF core-shell nanospheres were obtained after stirring for 8 h at 35 °C to obtain Si-C.

2.5. Characterizations

The phases and crystal structures of as-prepared samples were studied by powder X-ray diffraction (XRD) (Rigaku D/max2500 X-ray diffractometer with non-monochromated Cu Kα radiation) with a scanning range of 10° and 80° at a step size of 0.02°. The carbon content in the composite was measured by a sulfur carbon analyzer (CS600, USA). Raman spectrometer (LabRAM HR800, USA) was carried out to identify the graphitization degree of carbon in the composites. The specific surface areas and pore size distributions of the samples were tested by nitrogen adsorption-desorption measurements (ASAP 2460, Micromeritic Instruments, USA). The morphologies and nanostructures of the samples were detected by field-emission scanning electron microscopy (FESEM, FEI Nova NanoSEM 230, USA) and transmission electron microscopy (TEM, JEOL-JEM-2100F, Japan).

2.6. Electrochemical measurements

The working electrodes were prepared by dispersing the active materials, super P and sodium carboxymethyl cellulose (CMC) binder in de-ionized water at a weight ratio of 8:1:1 to form slurry. Thereafter, the slurry was coated on a copper foil and dried in a vacuum oven at 100 °C overnight. CR2016 coin cells were assembled in a glove-box (Mbraun, Garching, Germany) filled with pure argon. Lithium foil was used as the counter electrode, 1 mol L^{-1} $LiPF_6$ in ethyl carbonate/dimethyl carbonate/diethyl carbonate (EC/DMC/DEC, 1:1:1, in volume) with 10 wt% of fluoroethylene carbonate (FEC) as the electrolyte and polypropylene as the separator. The mass loading of electrode is about 1.0 mg cm^{-2}. The electrolyte amount in a cell is around 0.3 mL. Cyclic voltammetry (CV, 0.005–1.5 V, 0.1 mV s^{-1}) measurements were carried out on an electrochemical workstation (CHI660E, China). Galvanostatic charge/discharge was performed on a Land tester (Land CT 2001A, China) in the voltage range of 0.005–1.5 V (vs. Li/Li^+). All the capacities of cells have been calculated based on the whole mass of silicon and carbon. The electrochemical impedance spectrometry (EIS) was conducted with a Zahner-IM6ex electrochemical workstation (Zahner Co., Germany) in the frequency range of 100 kHz to 10 MHz.

3. Results and discussion

The synthesis process is schematically presented in Fig. 1. The SiO_2 nanospheres and PAN polymer were dispersed in DMF solution to form a homogenous dispersion by ultrasonication process. The obtained dispersion was electrospun into necklace-like SiO_2@polymer nanofibers. During this process, the SiO_2 nanospheres are coated by PAN polymer to form a core-shell structure. After magnesiothermic (Mg) reduction in inert atmosphere of Ar, the inner SiO_2 nanospheres are in-situ converted into mesoporous Si nanoparticles, whereas the exterior polymer shells are transformed into N-doped carbon shell. The PAN polymer functions as linker of the necklace-like structure and also serves as both carbon and nitrogen sources. The linked necklace-like carbon wrapped Si nanospheres can improve the structural stability of the electrode materials. Moreover, the carbonaceous material and the mesoporous structure can facilitate the electron transportation and electrolyte penetration.

The monodispersed SiO_2 nanospheres prepared by Stöber method were very uniform with a diameter of about 500 nm (Fig. S1a and b online). After electrospun, the SiO_2 nanospheres are linked by PAN polymers to form necklace-like fibers (Fig. S2a and b online). The SiO_2 nanospheres are neck-by-neck linked, which suggests the high loading of SiO_2 in the composite. Fig. 2 shows the morphology and interior structure of the obtained NL-Si@C-0.5 after Mg reduction. The energy dispersive X-ray (EDX) result (Fig. S3a and b online) shows that Mg element has been totally removed from the NL-Si@C-0.5 after water and HCl washing. The morphology of necklace-like network (Fig. 2a) was well preserved and no obvious structural collapse is observed. A higher magnification image (Fig. 2b) reveals the detailed information of the typical necklace-like structure. Adjacent Si nanospheres are continuously linked by carbon layers. The TEM image in Fig. 2c shows that the mesoporous Si nanospheres are encapsulated in necklace-like carbon shells. The bright part in the nanospheres (Fig. 2d) further confirms the porous structure of the NL-Si@C-0.5 composite. Fig. 2e shows a high-resolution TEM image of NL-Si@C-0.5, in which lattice strings with a fringe spacing of 0.32 nm are observed, corresponding to the (1 1 1) plane of Si. Additionally, a graphitized carbon layer with a thickness of around 10 nm is detected. The spatial distribution of different elements is shown by the elemental mapping (Fig. 2f). The result shows that Si is homogeneously distributed in the nanospheres. However, C and N elements are mainly distributed on the edges of the nanospheres, verifying the existence of carbon shells in the NL-Si@C-0.5 composite. Fig. S4 (online) shows the morphology of the Si-S. The result reveals that spherical morphology is preserved well and solid SiO_2 nanospheres are converted to porous Si nanospheres after Mg reduction process. According to Fig. S5 (online), the carbon layers and interior porous Si nanoparticles for Si-C can be clearly found. The morphology and structure of the carbon shells are further investigated by etching the NL-Si@C-0.5 composite with 10% HF solution. The XRD pattern (Fig. S6 online) of the sample after etching confirms complete removal of Si. TEM image (Fig. 2g) shows that the necklace-like structure is preserved well after etching. A higher magnification image (Fig. 2h) reveals that the adjacent carbon shells are linked by a thin carbon layer. Fig. 2i further shows that the interconnected carbon shells have high porosity, which could be ascribed to the catalysis of Mg during Mg reduction process. Compared to isolated carbon shells, the unique necklace-like carbon shells network can not only be easier for the ions and electrons transportation between adjacent carbon shells, but also avoid the loss of contact upon cycling.

In particular, the weight percentage of Si nanospheres in the composite and their distances are controllably adjusted by different addition of SiO_2 nanospheres. When 0.1 g SiO_2 nanospheres were added, the obtained NL-Si@C-0.1 network keeps a morphology of nanofibers (Fig. 3a). TEM image (Fig. 3b) further reveals that the mesoporous Si nanospheres are embedded into solid carbon fibers, forming pea-pod like structure. Increasing the addition

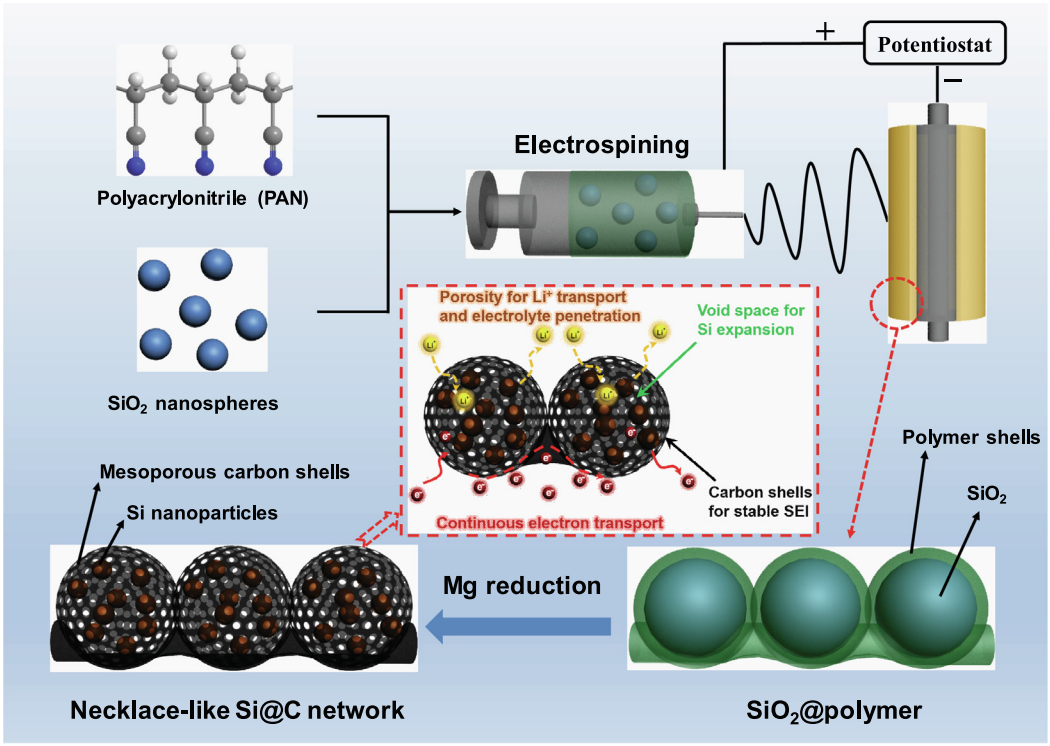

Fig. 1. (Color online) Schematic illustration of the synthesis process for necklace-like Si@C network.

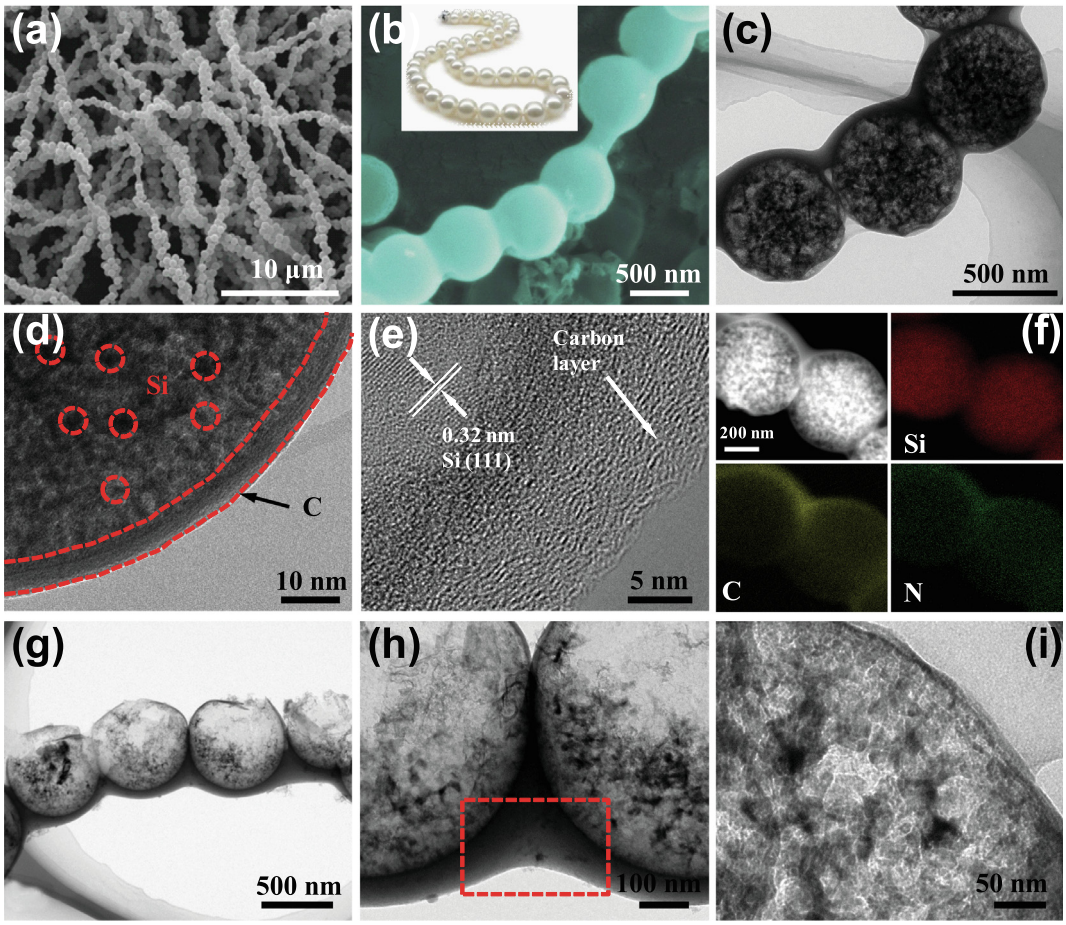

Fig. 2. (Color online) Morphologies and interior structures of NL-Si@C-0.5 and carbon shells. (a, b) Different magnification SEM images of NL-Si@C-0.5. (c–e) Low and high magnification TEM images of NL-Si@C-0.5. (f) High-angle annular dark field scanning transmission electron microscopy (HAADF-STEM) and element mapping images of NL-Si@C-0.5. (g–i) Low and high magnification TEM images of the necklace-like carbon shells after removal of Si nanoparticles.

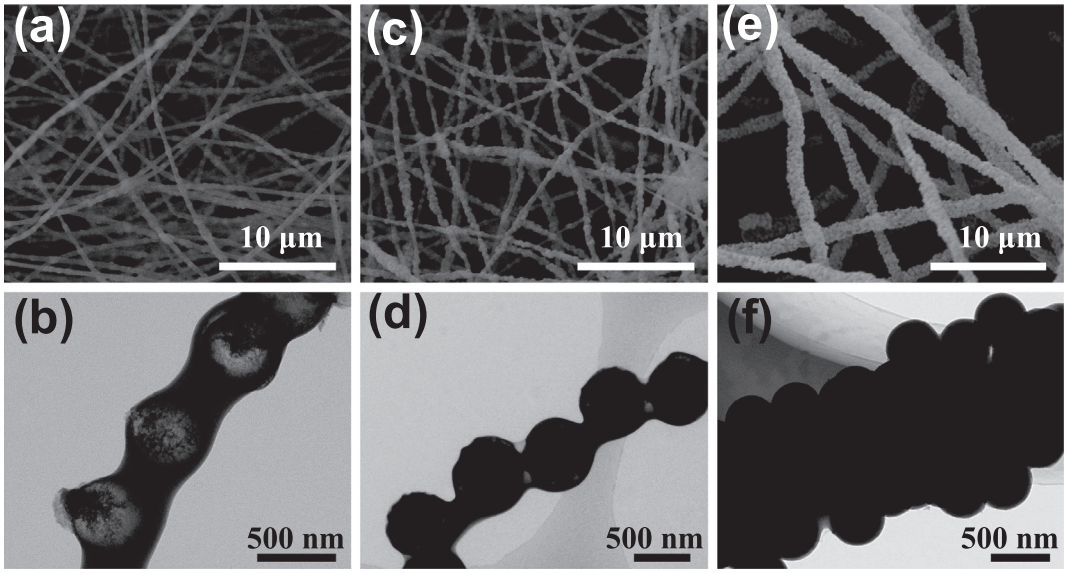

Fig. 3. SEM (a, c, e) and TEM (b, d, f) images of NL-Si@C-0.1 (a, b), NL-Si@C-0.3 (c, d), NL-Si@C-0.7 (e, f), respectively.

amount of SiO_2 nanospheres to 0.3 g, the adjacent mesoporous Si nanospheres are more closely distributed, but with detectable neighboring space (Fig. 3c, d). However, if the addition amount of SiO_2 nanospheres are increased to 0.7 g, the Si@C nanospheres are tightly stacked together to construct thick fibers with a diameter of around 1 μm (Fig. 3e). Moreover, the carbon shells cannot

be uniformly formed on the surface of the Si nanospheres (Fig. 3f). The result demonstrates that the carbon wrapping effect on the morphology and structure is greatly influenced by the addition amount of SiO_2 nanospheres during the electrospun process.

XRD analysis was performed to identify the crystalline structures of NL-Si@C-0.5 and Si-S. As shown in Fig. 4a, the peaks located at 28.4°, 47.3°, 56.1°, 69.1° and 76.3° are in good agreement with the standard pattern of Si (JCPDS No. 27-1402). For NL-Si@C-0.5, an additional broad peak at around 23° is related to (0 0 2) plane of amorphous carbon [39]. The carbon content in the composite is measured by a sulfur carbon analyzer and the corresponding values of NL-Si@C-0.1, NL-Si@C-0.3, NL-Si@C-0.5 and NL-Si@C-0.7 are 56.84%, 26.02%, 21.79%, 10.75%, respectively. Therefore, the Si content of NL-Si@C-0.1, NL-Si@C-0.3, NL-Si@C-0.5 and NL-Si@C-0.7 are 43.16%, 73.98%, 78.21%, 89.25%, respectively. In addition, Raman spectrum was conducted to evaluate the graphitic feature of NL-Si@C-0.5 (Fig. 4b). A peak located at around 510 cm^{-1} is related to the characteristic Si Raman band. Another two broad peaks at around 1,320 and 1,590 cm^{-1} are assigned to D band from sp^3-type disordered carbon and G band from sp^2-type graphitic carbon, respectively. The I_D/I_G ratio of NL-Si@C-0.5 is 1.06, much higher than that of the sample without adding Mg powders during heat treatment (Fig. S7 online), indicating that the carbon of NL-Si@C-0.5 has a higher graphitization [46]. Therefore, the graphitization degree of carbon can be enhanced by Mg reduction annealing process. Nitrogen isothermal adsorption/desorption measurement was carried out to further investigate the porosity of the necklace-like mesoporous Si@C composite. As shown in Fig. 4c, a type-IV curve with H3 hysteresis loops is obtained, indicating a typical mesoporous structure [47]. The Brunauer-Emmett-Teller (BET) surface area and total pore volume of NL-Si@C-0.5 are calculated to be 269.46 $m^2\ g^{-1}$ and 0.56 $cm^3\ g^{-1}$, respectively. Based on the Barrett-Joyner-Halenda (BJH) model, the pore size distribution is mainly in the range of 4–20 nm. X-ray photoelectron spectroscopy (XPS) was conducted to study the elements and valence states of the NL-Si@C-0.5. The full survey spectra (Fig. 4d) shows the N 1s, C 1s, Si 2p peaks in the NL-Si@C-0.5 composite. The fitting N 1s spectrum (Fig. 4e) can be resolved into three components located at about 398.8, 400.3 and 400.8 eV, corresponding to pyridinic N, pyrrolic N and graphitic N, respectively [48]. The N content in the composite is 1.62%. The existence of N can produce extrinsic defects and improve electric conductivity. The C 1s (Fig. 4f) spectrum is deconvoluted into C–C, C–N and C–O, respectively [39].

Fig. 5 shows the electrochemical performances of the mesoporous Si@C nanofiber composites as an anode for LIBs. Fig. 5a displays the representative first three consecutive CV curves of the NL-Si@C-0.5 at a scanning rate of 0.1 mV s^{-1} between 0.005 and 1.5 V. In the first cycle, only one cathodic peak below 0.1 V has been observed, corresponding to the generation of a SEI film and the alloying reaction of Si [49]. There are two anodic peaks located at around 0.34 and 0.51 V, ascribed to the delithiation of the Li-Si alloys [50]. In the followed cycles, the similar anodic peaks demonstrate good reversible capability. Furthermore, the CV peak intensity increase slightly in the first three cycles, indicating an activation process of the composite [51]. Fig. 5b shows the charge-discharge curves of NL-Si@C-0.5 for 1st, 2nd, 20th, and 50th cycles at 100 mA g^{-1}. The first discharge profile shows long plateaus below 0.2 V, which can be ascribed to the lithiation process of crystalline Si and the formation of SEI layer on the electrode. From second cycle to 50th cycle, the charge and discharge profiles are similar, indicating the formation of stable SEI layer and improved cycling stability for the later cycles. Fig. 5c shows the cycling performances of the obtained mesoporous Si@C composites with different Si content. Compared to NL-Si@C-0.1 and NL-Si@C-0.3 samples, the NL-Si@C-0.5 delivers higher reversible capacities, which can be attributed to higher weight percentages of Si in the composites. The NL-Si@C-0.5 exhibits a high capacity of 1,422.5 mAh g^{-1} and has a capacity retention of 72.5% after 50 cycles. However, further increasing the Si content in the composite (NL-Si@C-0.7), the capacity retention become unfavorable. Although the NL-Si@C-0.7 delivers a highest initial capacity of 1,742.2 mAh g^{-1}, only 753.1 mAh g^{-1} can be retained after 50 cycles. The fast capacity fading for NL-Si@C-0.7 can be attributed to the un-uniform carbon coating shells, which can not effectively tolerate the volume expansion of Si and avoid the direct reaction between Si and electrolyte. The bare silicon nanospheres and isolated silicon carbon nanospheres show worse cycling performance

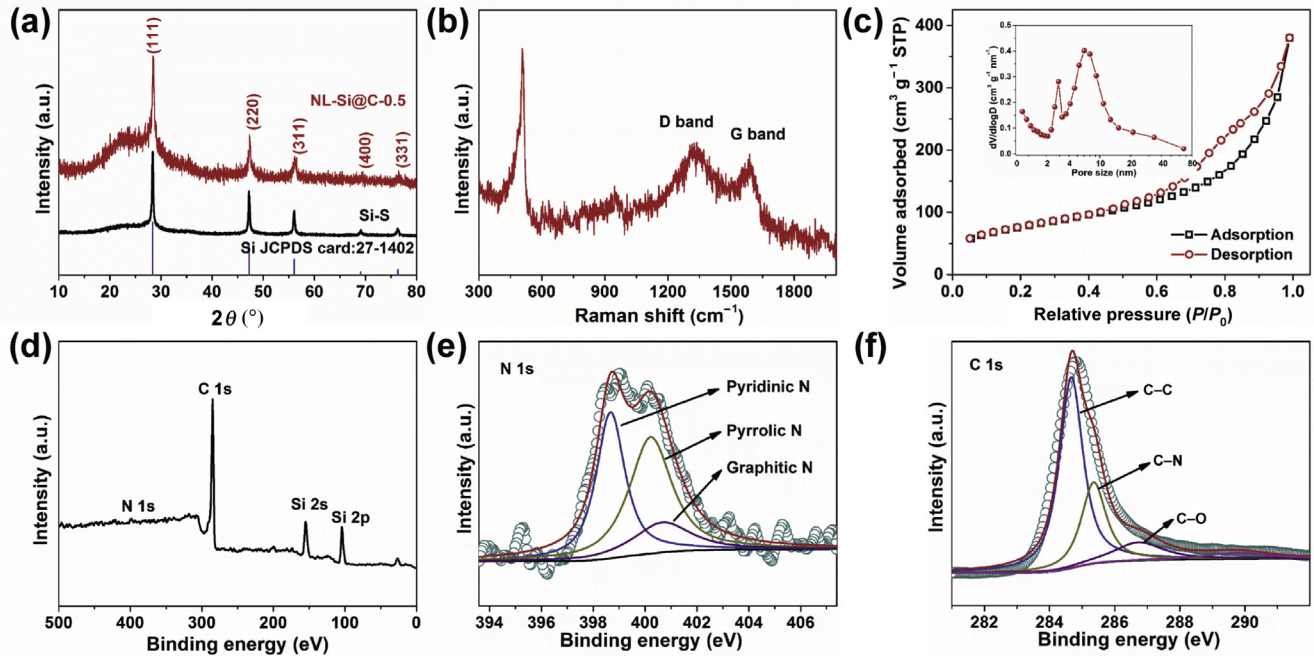

Fig. 4. (Color online) Structural characterizations of the obtained samples. (a) XRD patterns of NL-Si@C-0.5 and Si-S. (b) Raman spectrum. (c) Nitrogen adsorption-desorption isotherm. Inset: the corresponding pore size distribution. (d) Survey XPS spectrum. High-resolution N 1s (e) and C 1s (f) XPS spectrum of NL-Si@C-0.5.

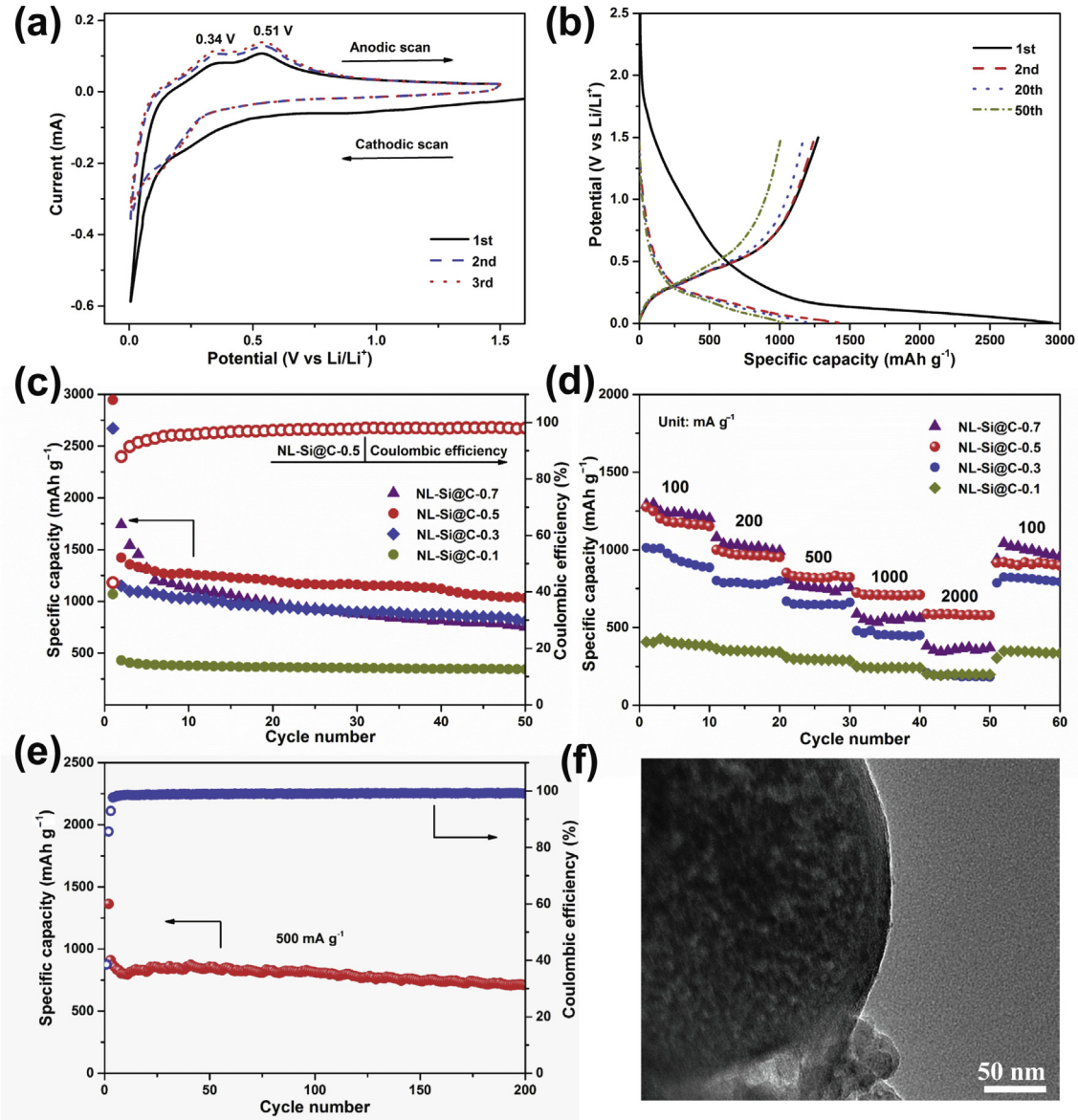

Fig. 5. (Color online) Electrochemical performances of the obtained samples. (a) The first three successive CV curves of NL-Si@C-0.5 at a scan rate of 0.1 mV s^{-1} in the potential of 0.005–1.5 V (vs. Li/Li^+). (b) Charge-discharge profiles of NL-Si@C-0.5 at 100 mA g^{-1}. (c) Cycling performances. (d) Rate capabilities of NL-Si@C-0.1, NL-Si@C-0.3, NL-Si@C-0.5, NL-Si@C-0.7. (e) Long-term cycling stability of NL-Si@C-0.5 at 500 mA g^{-1}. (f) TEM image of NL-Si@C-0.5 after 200 cycles at 500 mA g^{-1}.

than NL-Si@C-0.5 (Fig. S8 online). Fig. 5d shows the rate performances of the obtained NL-Si@C electrodes after running at 50 mA g^{-1} for 10 cycles to stabilize the electrodes. The NL-Si@C-0.5 delivers best rate capability with reversible capacities of 1175.3, 967.7, 819.3, and 708.5, and 586.2 mAh g^{-1} at 0.1, 0.2, 0.5, 1, and 2 A g^{-1}, respectively. In particular, the NL-Si@C-0.5 can still remain a capacity of 586.2 mAh g^{-1} at 2 A g^{-1}, much higher than that of NL-Si@C-0.7 (358.7 mAh g^{-1}), NL-Si@C-0.3 (189.7 mAh g^{-1}), and NL-Si@C-0.1 (197.6 mAh g^{-1}). When the current density is returned to 0.1 A g^{-1}, a capacity of 920.8 mAh g^{-1} can be recovered for NL-Si@C-0.5 electrode, indicating good rate capability. Furthermore, the NL-Si@C-0.5 shows good cycling stability of at high current density. As shown in Fig. 5e, the NL-Si@C-0.5 electrode remains a reversible capacity of 710 mAh g^{-1} after 200 cycles at 500 mA g^{-1}. Fig. 5f shows the TEM image of the NL-Si@C-0.5 after 200 cycles at 500 mA g^{-1}. The mesoporous Si@C nanospheres can be well preserved. Moreover, the carbon shells and interior Si nanoparticles can still be observed, demonstrating the excellent structural stability of NL-Si@C-0.5. The superior cycling stability and rate capability of NL-Si@C-0.5 can be ascribed to the fast ions and electrons transportation and the formation of stable SEI film, which are derived from unique necklace-like network structure and N-doped carbon wrapped mesoporous Si nanospheres. Yolk-shell Si@C structure can provide appropriate inner void space for the huge volume expansion of silicon during cycling, keeping a good structural integrity [36,52,53].

The electrochemical impedance spectroscopy (EIS) measurements were carried out to simulate the charge transfer resistance of the electrodes. Fig. S9 (online) shows the Nyquist plots and corresponding equivalent circuit model (inset) of the Si-S, Si-C, NL-Si@C-0.1 and NL-Si@C-0.5 electrodes. All samples consist of a semicircle in the high-frequency region and a following linear slope in the low-frequency region. The semicircle indicates charge transfer resistance (R_{ct}), whereas the line represents the Warburg impedance (Z_w) owing to diffusion-controlled process [54]. R_s refers to the resistance of electrolyte, current collectors and electrode materials. C_{PE} represents the double-layer capacitance and C_{int} could be ascribed to the capacitance caused by the

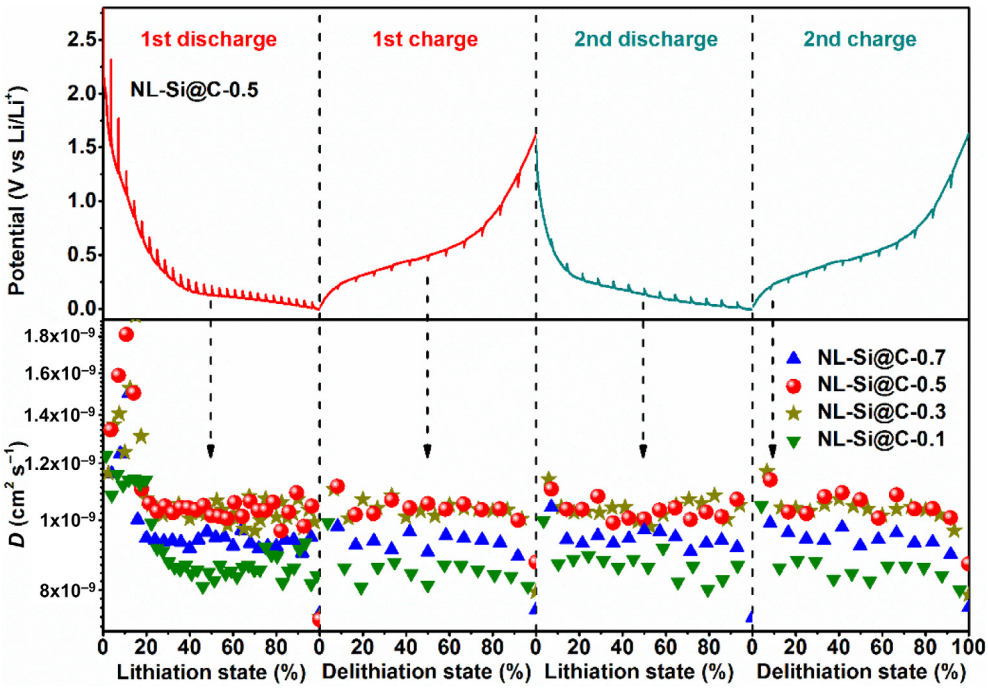

Fig. 6. (Color online) Charge-discharge GITT curves and lithium diffusion coefficient (D) for NL-Si@C-0.5 at 100 mA g^{-1} in the range of 0.005–1.5 V.

accumulation or loss of Li^+ in electrode material [55,56]. The R_{ct} values for Si-S, Si-C, NL-Si@C-0.1 and NL-Si@C-0.5 are calculated to be 673.2, 508.9, 349.1 and 204.1 Ω, respectively, suggesting the lowest charge-transfer resistance for NL-Si@C-0.5. The N-doped carbon shells network and yolk-shell structure of the NL-Si@C-0.5 guarantee fast charge transfer.

Galvanostatic intermittent titration technique (GITT) test was performed to further investigate the kinetics of Li solid-state diffusions in the NL-Si@C electrodes. This technique is based on chronopotentiometry and reveals multistep ion diffusivity into the composition dependent electrode kinetics [57]. The lithium diffusion coefficient (D) is calculated based on Eq. (1) as follows [58]:

$$D = \frac{4L^2}{\pi\tau}\left(\frac{\Delta E_s}{\Delta E_t}\right)^2, \quad (1)$$

where L (cm) is lithium ion diffusion length, for compact electrode, it is equal to thickness of electrode; τ (s) is the relaxation time; $2\Delta E_s$ (V) is the steady-state potential change by the current pulse. ΔE_t (V) is the potential change during the constant current pulse after eliminating the iR drop (Fig. S10 online). The obtained GITT curves and D values at various lithiation/delithiation states for NL-Si@C electrodes are shown in Fig. 6. The D in the NL-Si@C-0.5 ranges from 7.2×10^{-10} to 1.3×10^{-9} cm^2 s^{-1} during the first discharge process and ranges from around 8.5×10^{-10} to 1.1×10^{-9} cm^2 s^{-1} in the following cycles, much higher than that in NL-Si@C-0.1 and NL-Si@C-0.7, indicating an enhanced lithium ion diffusion in the bulk active electrode material. The highest lithium diffusivity for NL-Si@C-0.5 is mainly attributed to its necklace-like carbon shells network, which has a higher electric conductivity and provides numerous mesoporous channels and active sites for fast ion diffusion.

4. Conclusions

In summary, necklace-like Si@C nanofibers network has been successfully synthesized via electrospinning method followed by magnesiothermic reduction process. The mesoporous Si nanospheres are encapsulated in N-doped carbon shells, which are linked in chains to form a necklace-like structure. Importantly, the distance of adjacent Si@C nanospheres can be adjusted by different addition amounts of SiO_2 nanospheres. When used as anode materials for LIBs, NL-Si@C composites show better electrochemical performances than bare Si nanospheres and isolated Si-C nanospheres. Furthermore, NL-Si@C-0.5 shows best cycling stability and rate capability compared to other NL-Si@C composites. These results suggest that necklace-like network structure could improve lithium storage properties of Si-based materials. This structural design could also be extended to other materials used as active materials for lithium ion batteries, sodium ion batteries, supercapacitors and electro-catalysis.

Conflict of interest

The authors declare that they have no conflict of interest.

Acknowledgments

This work was supported by the National Key Research and Development Program of China (2018YFB0104200).

Appendix A. Supplementary data

Supplementary data to this article can be found online at https://doi.org/10.1016/j.scib.2019.01.015.

References

[1] Xu Q, Sun JK, Li JY, et al. Scalable synthesis of spherical Si/C granules with 3D conducting networks as ultrahigh loading anodes in lithium-ion batteries. Energy Storage Mater 2018;12:54–60.
[2] Liu Z, Chang X, Wang T, et al. Silica-derived hydrophobic colloidal nano-Si for lithium-ion batteries. ACS Nano 2017;11:6065–73.
[3] Liang S, Cao X, Wang Y, et al. Uniform $8LiFePO_4 \cdot Li_3V_2(PO_4)_3$/C nanoflakes for high-performance Li-ion batteries. Nano Energy 2016;22:48–58.
[4] Tang C, Liu Y, Xu C, et al. Ultrafine nickel-nanoparticle-enabled SiO_2 hierarchical hollow spheres for high-performance lithium storage. Adv Funct Mater 2018;28:1704561.

[5] Xu Q, Sun JK, Yin YX, et al. Facile synthesis of blocky SiO_x/C with graphite-like structure for high-performance lithium-ion battery anodes. Adv Funct Mater 2017;28:1705235.
[6] Li S, Tang H, Ge P, et al. Electrochemical investigation of natural ore molybdenite (MoS_2) as a first-hand anode for lithium storages. ACS Appl Mater Interfaces 2018;10:6378–89.
[7] Zhang N, Chen C, Yan X, et al. Bacteria-inspired fabrication of Fe_3O_4-carbon/graphene foam for lithium-ion battery anodes. Electrochim Acta 2017;22:339–46.
[8] Liang J, Yuan C, Li H, et al. Growth of SnO_2 nanoflowers on N-doped carbon nanofibers as anode for Li- and Na-ion batteries. Nano Micro Lett 2018;10:21.
[9] Xu Q, Li JY, Sun JK, et al. Watermelon-inspired Si/C microspheres with hierarchical buffer structures for densely compacted lithium-ion battery anodes. Adv Energy Mater 2017;7:1601481.
[10] Jin Y, Li S, Kushima A, et al. Self-healing SEI enables full-cell cycling of a silicon-majority anode with a coulombic efficiency exceeding 99.9%. Energy Environ Sci 2017;10:580–92.
[11] Jeong MG, Du HL, Islam M, et al. Self-rearrangement of silicon nanoparticles embedded in micro-carbon sphere framework for high-energy and long-life lithium-ion batteries. Nano Lett 2017;17:5600–6.
[12] Nie P, Le Z, Chen G, et al. Graphene caging silicon particles for high-performance lithium-ion batteries. Small 2018;14:1800635.
[13] Huang S, Zhang L, Liu L, et al. Rationally engineered amorphous TiO_x/Si/TiO_x nanomembrane as an anode material for high energy lithium ion battery. Energy Storage Mater 2018;12:23–9.
[14] Xu Q, Li JY, Yin YX, et al. Nano/micro-structured Si/C anodes with high initial coulombic efficiency in Li-ion batteries. Chem Asia J 2016;11:1205–9.
[15] Kim SY, Lee J, Kim BH, et al. Facile synthesis of carbon-coated silicon/graphite spherical composites for high-performance lithium-ion batteries. ACS Appl Mater Interfaces 2016;8:12109–17.
[16] Casimir A, Zhang H, Ogoke O, et al. Silicon-based anodes for lithium-ion batteries: effectiveness of materials synthesis and electrode preparation. Nano Energy 2016;27:359–76.
[17] Chan CK, Peng H, Liu G, et al. High-performance lithium battery anodes using silicon nanowires. Nat Nanotechnol 2008;3:31–5.
[18] Yu X, Xue F, Huang H, et al. Synthesis and electrochemical properties of silicon nanosheets by DC arc discharge for lithium-ion batteries. Nanoscale 2014;6:6860–5.
[19] Hieu NS, Lim JC, Lee JK. Free-standing silicon nanorods on copper foil as anode for lithium-ion batteries. Microelectron Eng 2012;89:138–40.
[20] Yao Y, McDowell MT, Ryu I, et al. Interconnected silicon hollow nanospheres for lithium-ion battery anodes with long cycle life. Nano Lett 2011;11:2949–54.
[21] Stokes K, Geaney H, Flynn G, et al. Direct synthesis of alloyed $Si_{1-x}Ge_x$ nanowires for performance-tunable lithium ion battery anodes. ACS Nano 2017;11:10088–96.
[22] Li W, Guo X, Lu Y, et al. Amorphous nanosized silicon with hierarchically porous structure for high-performance lithium ion batteries. Energy Storage Mater 2017;7:203–8.
[23] Hou G, Cheng B, Cao Y, et al. Scalable production of 3D plum-pudding-like Si/C spheres: towards practical application in Li-ion batteries. Nano Energy 2016;24:111–20.
[24] Zhang YC, You Y, Xin S, et al. Rice husk-derived hierarchical silicon/nitrogen-doped carbon/carbon nanotube spheres as low-cost and high-capacity anodes for lithium-ion batteries. Nano Energy 2016;25:120–7.
[25] Li JY, Xu Q, Li G, et al. Research progress regarding Si-based anode materials towards practical application in high energy density Li-ion batteries. Mater Chem Front 2017;1:1691–708.
[26] Zhang Y, Pan A, Ding L, et al. Nitrogen-doped yolk-shell-structured CoSe/C dodecahedra for high-performance sodium ion batteries. ACS Appl Mater Interfaces 2017;9:3624–33.
[27] Zhu M, Kong X, Yang H, et al. One-dimensional coaxial Sb and carbon fibers with enhanced electrochemical performance for sodium-ion batteries. Appl Surface Sci 2018;428:448–54.
[28] Hou H, Shao L, Zhang Y, et al. Large-area carbon nanosheets doped with phosphorus: a high-performance anode material for sodium-ion batteries. Adv Sci 2017;4:1600243.
[29] Zhang Y, Foster CW, Banks CE, et al. Graphene-rich wrapped petal-like rutile TiO_2 tuned by carbon dots for high-performance sodium storage. Adv Mater 2016;28:9391–9.
[30] Shen X, Tian Z, Fan R, et al. Research progress on silicon/carbon composite anode materials for lithium-ion battery. J Energy Chem 2018;27:1067–90.
[31] Xu Z, Gang Y, Garakani M, et al. Carbon-coated mesoporous silicon microsphere anodes with greatly reduced volume expansion. J Mater Chem A 2016;4:6098–106.
[32] Kim B, Ahn J, Oh Y, et al. Highly porous carbon-coated silicon nanoparticles with canyon-like surfaces as a high-performance anode material for Li-ion batteries. J Mater Chem A 2018;6:3028–37.
[33] Xu Y, Zhu Y, Han F, et al. 3D Si/C fiber paper electrodes fabricated using a combined electrospray/electrospinning technique for Li-ion batteries. Adv Energy Mater 2015;5:1400753.
[34] Chen SQ, Shen LF, Aken PA, et al. Dual-functionalized double carbon shells coated silicon nanoparticles for high performance lithium-ion batteries. Adv Mater 2017;29:1605650.
[35] Liu Z, Guan D, Yu Q, et al. Monodisperse and homogeneous SiO_x/C microspheres: a promising high-capacity and durable anode material for lithium-ion batteries. Energy Storage Mater 2018;13:112–8.
[36] Yang J, Wang YX, Chou SL, et al. Yolk-shell silicon-mesoporous carbon anode with compact solid electrolyte interphase film for superior lithium-ion batteries. Nano Energy 2015;18:133–42.
[37] Liu W, Jiang J, Wang H, et al. Influence of graphene oxide on electrochemical performance of Si anode material for lithium-ion batteries. J Energy Chem 2016;25:817–24.
[38] Xiao Z, Xia N, Song L, et al. Synthesis of yolk-shell-structured Si@C nanocomposite anode material for lithium-ion battery. J Electron Mater 2018;47:6311–8.
[39] Xu R, Wang G, Zhou T, et al. Rational design of Si@carbon with robust hierarchically porous custard-apple-like structure to boost lithium storage. Nano Energy 2017;39:253–61.
[40] Lu C, Wang D, Zhao J, et al. A continuous carbon nitride polyhedron assembly for high-performance flexible supercapacitors. Adv Funct Mater 2017;27:1606219.
[41] Liang J, Gao X, Guo J, et al. Electrospun MoO_2@NC nanofibers with excellent Li^+/Na^+ storage for dual applications. Sci China Mater 2017;61:30–8.
[42] Hou H, Banks CE, Jing M, et al. Carbon quantum dots and their derivative 3D porous carbon frameworks for sodium-ion batteries with ultralong cycle life. Adv Mater 2015;27:7861–6.
[43] Li Z, Fang Y, Zhang J, et al. Necklace-like structures composed of Fe_3N@C yolk-shell particles as an advanced anode for sodium-ion batteries. Adv Mater 2018;30:1800525.
[44] Li Z, Guan B, Zhang J, et al. A compact nanoconfined sulfur cathode for high-performance lithium-sulfur batteries. Joule 2017;1:576–87.
[45] Stöber W, Fink A, Bohn E. Controlled growth of monodisperse silica spheres in the micron size range. J Colloid Interfaces Sci 1968;26:62–9.
[46] Zhang Y, Pan A, Wang Y, et al. Self-templated synthesis of N-doped $CoSe_2$/C double-shelled dodecahedra for high-performance supercapacitors. Energy Storage Mater 2017;8:28–34.
[47] Wang Y, Zhu T, Zhang Y, et al. Rational design of multi-shelled CoO/Co_9S_8 hollow microspheres for high-performance hybrid supercapacitors. J Mater Chem A 2017;5:18448–56.
[48] Kim SJ, Kim MC, Han SB, et al. 3D flexible Si based-composite (Si@Si_3N_4)/CNF electrode with enhanced cyclability and high rate capability for lithium-ion batteries. Nano Energy 2016;27:545–53.
[49] An Y, Fei H, Zeng G, et al. Scalable, and controllable fabrication of nanoporous silicon from commercial alloy precursors for high-energy lithium-ion batteries. ACS Nano 2018;12:4993–5002.
[50] Liang G, Qin X, Zou J, et al. Electrosprayed silicon-embedded porous carbon microspheres as lithium-ion battery anodes with exceptional rate capacities. Carbon 2018;127:424–31.
[51] Zuo X, Xia Y, Ji Q, et al. Self-templating construction of 3D hierarchical macro-/mesoporous silicon from 0D silica nanoparticles. ACS Nano 2017;11:889–99.
[52] Gattu B, Epur R, Jampani PH, et al. Silicon-carbon core-shell hollow nanotubular configuration high-performance lithium-ion anodes. J Phys Chem C 2017;121:9662–71.
[53] Zou G, Hou H, Cao X, et al. 3D hollow porous carbon microspheres derived from Mn-MOFs and their electrochemical behavior for sodium storage. J Mater Chem A 2017;5:23550–8.
[54] Kong X, Zhu T, Cheng F, et al. Uniform $MnCo_2O_4$ porous dumbbells for lithium-ion batteries and oxygen evolution reactions. ACS Appl Mater Interfaces 2018;10:8730–8.
[55] Wang Q, Zhang W, Guo C, et al. In situ construction of 3D interconnected FeS@Fe_3C@graphitic carbon networks for high-performance sodium-ion batteries. Adv Funct Mater 2017;27:1703390.
[56] Ge P, Hou H, Banks CE, et al. Binding $MoSe_2$ with carbon constrained in carbonous nanosphere towards high-capacity and ultrafast Li/Na-ion storage. Energy Storage Mater 2018;12:310–23.
[57] Pei C, Xiong F, Sheng J, et al. VO_2 nanoflakes as the cathode material of hybrid magnesium-lithium-ion batteries with high energy density. ACS Appl Mater Interfaces 2017;9:17060–6.
[58] Ngo DT, Le H, Kim C, et al. Mass-scalable synthesis of 3D porous germanium–carbon composite particles as an ultra-high rate anode for lithium ion batteries. Energy Environ Sci 2015;8:3577–88.

Xiangzhong Kong is a postdoctoral researcher supervised by Prof. Anqiang Pan. He received his Ph.D. degree in School of Materials Science and Engineering from Central South University in 2018. His research interest is Mn-based and Si-based anode materials for lithium-ion batteries.

Anqiang Pan is a Sheng-Hua Professor of Central South University. Before joining Central South University, he worked at University of Washington, Pacific Northwest National Laboratory and Nanyang Technological University consequently. His current interests focus on the synthesis of nanostructured materials for energy storage applications, including batteries, supercapacitors and catalysts.